Special Sensor Microwave/Imager (SSM/I) Observations of Hurricane Hugo (1989)

RANDALL J. ALLISS AND SETHU RAMAN

Department of Marine, Earth and Atmospheric Sciences, North Carolina State University, Raleigh, North Carolina

SIMON W. CHANG

Naval Research Laboratory, Washington, D.C.

(Manuscript received 21 November 1991, in final form 25 March 1992)

ABSTRACT

Data from the Special Sensor Microwave/Imager (SSM/I) on board a Defense Meteorological Satellite Program (DMSP) spacecraft have been used to study the precipitation patterns associated with Hurricane Hugo (1989). Results indicate the intensification of Hugo was associated with increases in SSM/I-derived total latent heat release and increases in heavier rainfall rates near the storm center. This study also shows that SSM/I rainfall rates prior to the landfall of Hugo at Charleston, South Carolina, compared favorably with raingage observations. Additionally, data from the 85-GHz channel was used to monitor the extent of convection near the storm's center. As Hugo intensified, the areal coverage of deep convection increased. Furthermore, the 85-GHz brightness-temperature imagery was useful in determining the location of Hugo's low-level center. These results indicate the potential of using SSM/I data in the analysis and prediction of tropical cyclones in an operational environment.

1. Introduction

Due to the scarcity of conventional, in situ meteorological data over the open oceans, passive microwave radiometry has the potential to become an important source of observations of tropical weather systems, especially tropical cyclones. The primary advantage of these instruments is that the microwave radiation can penetrate the overlying cirrus clouds with little attenuation, thereby revealing structural details—particularly those areas of deep convection—not always depicted by visible and infrared images. Recently, remote sensing of tropical cyclones from space has been enhanced via the Special Sensor Microwave/Imager (SSM/I), which rides on board a polar-orbiting Defense Meteorological Satellite Program (DMSP) spacecraft. The SSM/I is a joint U.S. Navy–Air Force operational instrument that measures critical atmospheric, oceanographic, and land parameters. Potential applications of SSM/I data to the operational analysis of tropical weather systems have been described by a number of recent papers (e.g., Felde and Glass 1991; Goodberlet et al. 1989; Negri et al. 1989; Rao et al. 1991; Rappaport 1991; Sandlin and Spangler 1989; Velden et al. 1989). Rappaport and Black (1989) point out important SSM/I limitations, such as relatively infrequent overpasses of tropical cyclones, navigational errors, and limitations imposed by poor spatial resolution of various SSM/I sensors.

It is well remembered that Hurricane Hugo made landfall at Charleston, South Carolina, and caused tremendous damage along the United States southeast coastal region, as well as in the Caribbean islands. In this paper, rainfall rates derived from algorithms using the brightness temperatures (BT) of radiation are used to examine the precipitation patterns observed in Hugo. Since the maintenance of tropical cyclones is dependent upon the release of latent heat, remote sensing of latent heat release becomes important. The use of passive microwave radiometry in observing the latent heat release in tropical cyclones was valuable in monitoring the moisture budget of these storms (Adler and Rodgers 1977). This study compares SSM/I-derived rainfall rates and other rainfall parameters with the observed intensity of the storm. Quantitative results of the spatial variations of the area-averaged rain rate in the inner and outer core regions of Hugo and their relationship to changes in storm-scale precipitation patterns are presented. SSM/I rainfall rates are also compared to raingage observations made near the path of Hugo during landfall in the Carolinas.

Accurate estimates of tropical cyclone centers are always important in storm analysis and prediction. Velden et al. (1989) indicated that the location of centers of cyclonic storms could be estimated with greater precision and consistency using 85-GHz imagery, compared to using conventional visible images, which

Corresponding author address: Dr. Sethu Raman, Department of Marine, Earth and Atmospheric Sciences, Box 8208, North Carolina State University, Raleigh, NC 27695-8202.

are limited by dense cloud overcast and by nighttime hours. When using the Geostationary Operational Environmental Satellite (GOES) imagery alone, there is occasionally great uncertainty in the location of tropical cyclone centers (Mayfield et al. 1988). Because microwave radiation at 85 GHz is sensitive to convective clouds and precipitation over oceanic regions, 85-GHz imagery is also examined to observe the storm structure as related to Hugo's intensity and to estimate the location of the center near the surface.

2. SSM/I characteristics and capabilities

Since its launch in June 1987, the first DMSP SSM/I has monitored the development and course of approximately 75% of the tropical storms and hurricanes that have occurred worldwide (Sandlin and Spangler 1989). The SSM/I completes 14.1 revolutions per day along a near-sun-synchronous track at an altitude of 833 km. It has an inclination angle of 98.8° and an orbital period of 102.0 min. The SSM/I uses a conical scanner with an angle of incidence of 53°. With an observational swath width of 1400 km, there is an 89% probability of viewing a storm in the tropics at least once per day. With the recent launch of the second SSM/I, this probability has increased to 99%, and the probability of at least two passes per day has increased to 89%. The chance of at least three passes per day is currently 59% (Velden et al. 1989). Figure 1 shows the coverage and orbital track of one SSM/I in 24 h. The shaded regions indicate possible data gaps in a 24-h period.

Radiation measured by the SSM/I comes from three sources—atmospheric emission, emission from the earth's surface, and atmospheric emission reflected from the earth's surface. For microwave radiation, significant attenuation can be caused by water vapor, oxygen, and liquid water (both in the form of cloud water and rain). Clouds or rain, however, also considerably increase the atmospheric emission. In extreme cases, clouds or rain totally obscure the surface, such that the microwave radiation is related only to atmospheric phenomena.

The SSM/I frequencies are 19.4, 22.2, 37.0, and 85.5 GHz. Through the proper choice of instrumental parameters (wavelength, polarization, and viewing angle), it is possible to establish useful relations between the BTs measured by the multifrequency radiometers and specific atmospheric parameters of interest. The rain-rate algorithm used in this study is described by Olson (1989) and Hollinger (1991). It was developed using a combination of the 85-GHz horizontal (H) and vertical (V), 37-GHz (V), 22-GHz (V) and (H), and the 19-GHz (V) channels. In general, the SSM/I observes a region of rain as an area of high BTs over the otherwise cold (in terms of BTs) ocean. The basis of the rain-rate algorithm over the ocean is that initially the 19- and 37-GHz BTs increase as rain rates increase

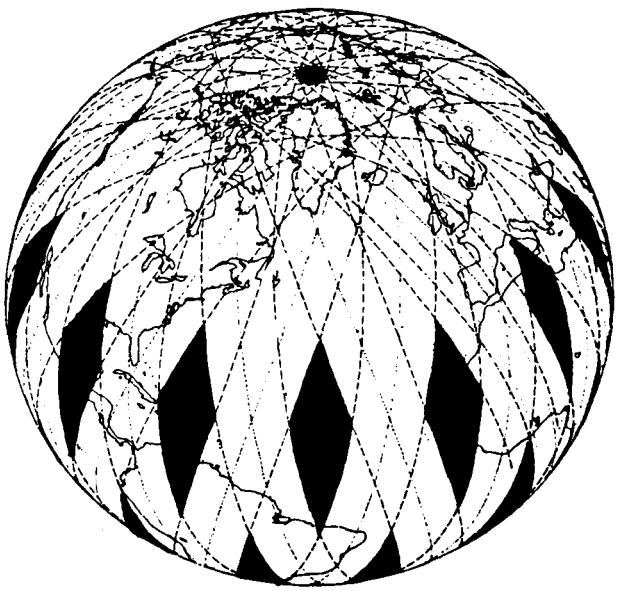

FIG. 1. Ground coverage of SSM/I in 24 h (from Hollinger 1989). Shaded areas indicated data gaps. Dashed lines indicate the boundaries of the swath. Dotted lines indicate the nadir.

up to a moderate rain rate, after which the BTs decrease as the rain rates increase further. This reduction in BTs for larger rain-rate values is due to the scattering by the large raindrops or to hail present in heavy rain, or both.

Hollinger (1991) describes the detailed procedure for determining rain rates from BTs. Pixels within ±100 km of the coast were not processed because the field of view contained data from both sea and land surfaces resulting in large gradients in the estimated fields over coastal regions. Fortunately, this problem was minimized in our study because all but one SSM/I swath covered the open oceans. Because the 85-GHz (H) channel was not operating during this period, an alternate algorithm was used. Following Hollinger (1991), rainfall rates over the ocean were computed using

$$R = \exp(5.10196 - 0.05378T_{37V} + 0.2766T_{37H} + 0.01373T_{19V}) - 2.0 \text{ mm h}^{-1}, \quad (1)$$

whereas for rainfall rates over land, we applied

$$R = \exp(-17.76849 - 0.09612T_{37V} + 0.15678T_{19V}) - 1.0 \text{ mm h}^{-1}, \quad (2)$$

where R is the rainfall rate and T_{85V}, T_{85H}, T_{37V}, T_{22V}, and T_{19V} are the BTs of the 85-GHz (V), 85-GHz (H), 37-GHz (V), 22-GHz (V), and 19-GHz (V) polarized channels, respectively. If the formulas produced a rainfall rate less than zero, then the rain-rate value was set to zero.

All SSM/I products have been statistically validated by comparisons with ground-truth measurements. In addition, all products are expected to be accurate within specification approximately 67% ($\pm 1\ \sigma$) of the time (Sandlin and Spangler 1989). The SSM/I specifications require 5 mm h^{-1} accuracy in standard deviation for rainfall-rate estimates between 0 and 25 mm h^{-1} (Hollinger 1991). There is an inherent uncertainty between 10 and 25 km in the registration of the image because of navigational errors (Sandlin 1991, personal communication). The SSM/I data used in this study were obtained through the Fleet Numerical Oceanographic Center and preprocessed at the Center for Advanced Space Sensing of the Naval Research Laboratory. Preprocessing entails resampling, smoothing, and projecting the data into grid format.

3. A synoptic description of Hurricane Hugo

As described in Case and Mayfield (1990), Hurricane Hugo, over the period of 10–22 September 1989, followed a course that was typical for North Atlantic tropical cyclones (Fig. 2). Hugo was detected by Meteorological Satellite (Meteosat) imagery on 9 September as an area of disturbed weather moving west off the coast of Africa. A tropical depression developed out of this disturbed area while moving westward across the tropical Atlantic. Embedded in the low-latitude easterlies, this depression strengthened and was named a tropical storm on 11 September by the National Hurricane Center (NHC). On 13 September, while still located some 3000 km east of the Caribbean Sea, the storm intensified to hurricane strength. On 15 September, U.S. Air Force reconnaissance aircraft made its first flight into the center of Hugo and found a minimum central pressure of 918 mb and maximum sustained surface winds of about 72 m s^{-1}. As Hugo approached the Leeward Islands, it slowed and began to turn toward the west-northwest. On 17 September, the center passed directly over the island of Guadeloupe. A turn toward the northwest followed as the center passed over St. Croix and over the eastern tip of Puerto Rico on 18 September. As Hugo exited the Caribbean, its movement maintained a general track toward the northwest. Figure 3 shows the minimum central pressure and maximum winds as a function of time obtained from NHC best-track data.

During the 30 h prior to landfall in South Carolina, Hugo began to accelerate toward the northwest. Final landfall occurred at 0400 UTC 22 September, just

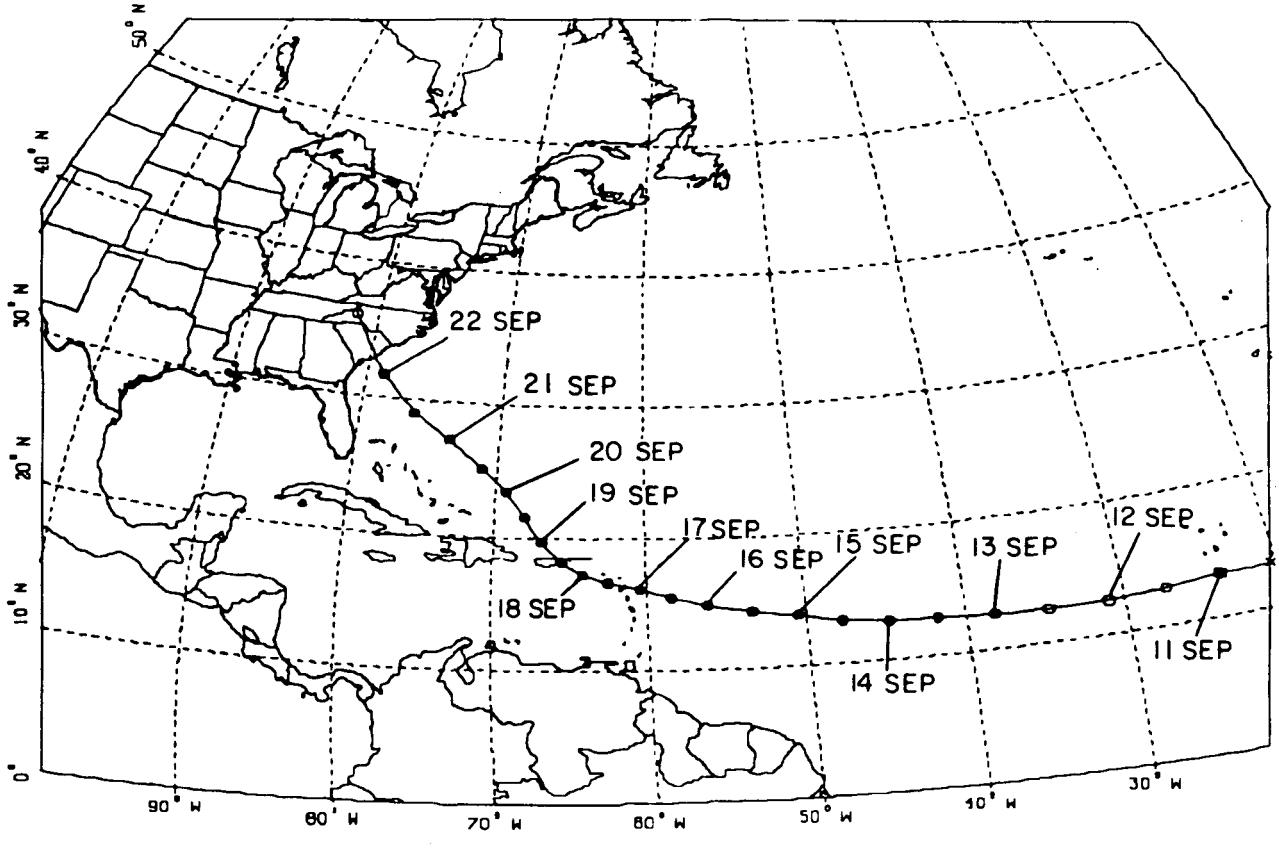

FIG. 2. Track of Hurricane Hugo from depression stage through final landfall: × = tropical depression stage, O = tropical storm stages, and ● = hurricane stages. Labels indicate location at 0000 UTC for each day.

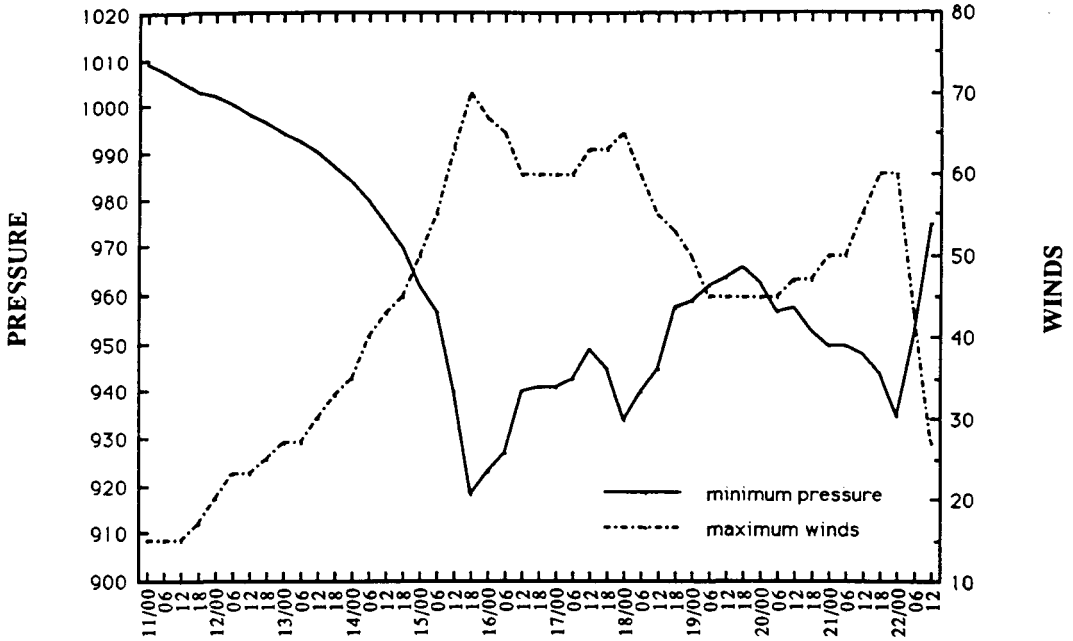

FIG. 3. Times series (UTC) of minimum central sea level pressure (mb) and maximum sustained wind speeds (m s^{-1}) obtained from NHC best-track data.

north of Charleston, South Carolina. Reintensification 30 h prior to landfall, along with a large translational speed, was responsible for the significant storm surge and severe damage along the South Carolina coastline. Based on U.S. Air Force reconnaissance reports, NHC estimated maximum sustained surface winds of 60 m s^{-1} just prior to landfall (Powell et al. 1991). By 1200 UTC 22 September, Hugo had weakened but maintained tropical-storm strength as it passed Charlotte, North Carolina. A turn toward the north occurred thereafter, and on 23 September, Hugo became extratropical in character (Case and Mayfield 1990).

4. Hugo precipitation pattern derived from SSM/I data

SSM/I observations were obtained from Hugo's predepression stage through final landfall. Figure 4a reveals SSM/I rain rates around 0700 UTC 10 September, just prior to Hugo's classification as a tropical depression. Two areas of convection with moderate rainfall rates (10–15 mm h^{-1}) were observed to the southeast of the Cape Verde Islands. Over the next 13 h, according to Meteosat imagery, the two areas of convection merged. SSM/I rain rates at 2000 UTC

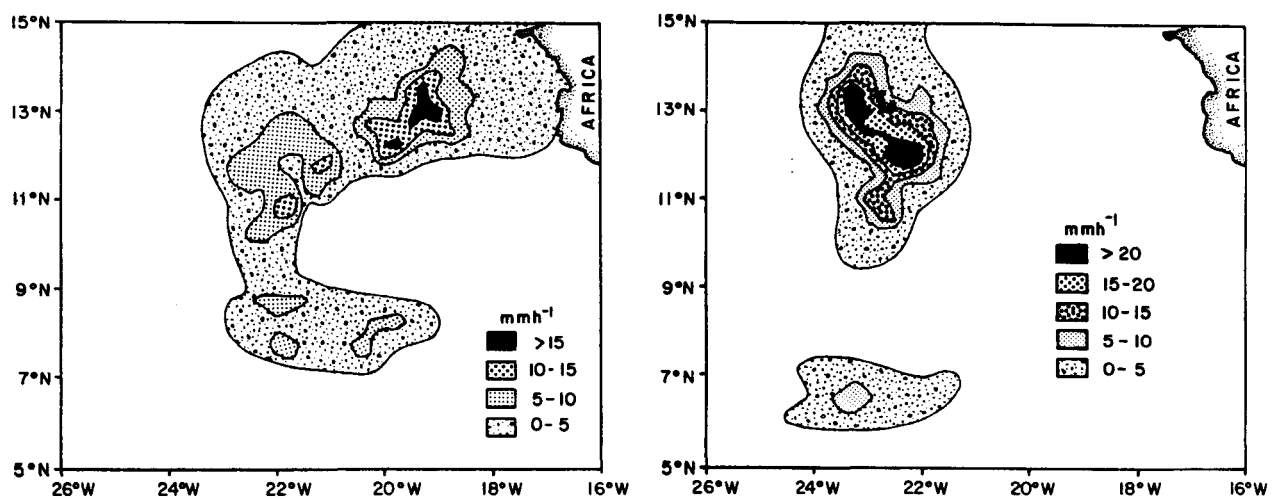

FIG. 4. (a) SSM/I rainfall rates at 0700 UTC 10 September. (b) Rainfall rates at 2000 UTC 10 September.

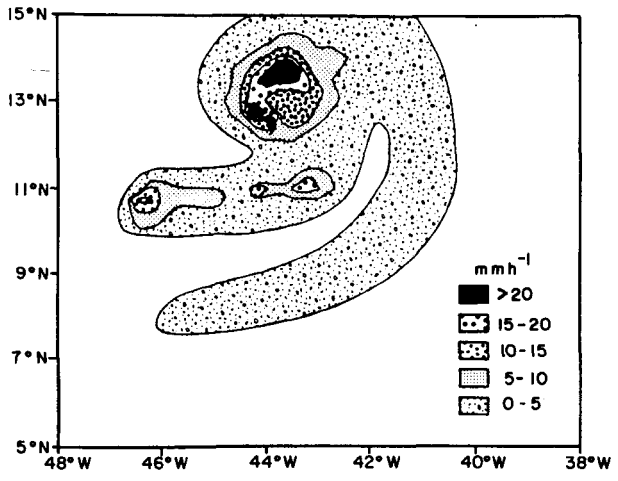

FIG. 5. SSM/I rainfall rates at 2100 UTC 13 September.

also showed one area of convection with some curvature in the rain pattern (Fig. 4b). Coverage by SSM/I was available 3 days later on 13 September. At this time, NHC had classified the storm as a hurricane with estimated maximum sustained winds of 33 m s^{-1}. The precipitation pattern showed an organized area of convection around the center of Hugo (Fig. 5). Figure 5 shows the approximate location of Hugo as determined from NHC best-track data. A large rainband also extended to the south and west of the storm's inner-core region. This rainband was several hundred kilometers long and approximately 100 km wide. This rainband was similar to those observed by Willoughby et al. (1984).

Hugo underwent a period of explosive deepening just prior to the arrival of the first NOAA P-3 aircraft on 15 September (Black and Marks 1991). The central pressure at 0900 UTC was estimated to be 949 mb, with maximum sustained winds near 60 m s^{-1} (see Fig. 3, Black and Marks 1991). SSM/I rain-rate imagery at 0900 UTC showed a large area of high rainfall rates associated with the inner-core region of the storm (Fig. 6a). What appeared to be an eyewall with high rain rates was also observed around the center, with the most intense precipitation (rates greater than 25 mm h^{-1}) occurring in the northwest region of the eyewall. The radius of the eyewall, measured using 85-GHz imagery, was 24 km. The SSM/I pass on 13 September did not show an eyewall or intense precipitation around its center, suggesting that the precipitation field was not as well organized. A spiral band at 0900 UTC was also evident in the rain-rate pattern to the north of the hurricane center. These bands curved inward toward the center of circulation. Their importance to intensity changes has been shown in Willoughby et al. (1982), who reported that large intensity changes can result from contraction and reformation of concentric, convective rings around the eye. SSM/I observations between 1000 UTC 10 September and 0900 UTC 15 September, if available to forecasters, may have assisted in the analysis of Hugo since airborne reconnaissance was not available.

The scene at 2200 UTC 15 September captured Hugo at near maximum intensity. According to U.S. Air Force reconnaissance, a central pressure of 918 mb and sustained winds in excess of 70 m s^{-1} were observed just prior to the SSM/I observation (see Fig. 3, Black and Marks 1991). Figure 6b reveals an intense and tightly wrapped eyewall with a radius of 9 km as measured from the 85-GHz imagery. There is also the presence of a concentric ring at a radius of 91 km from the center. It appears that this concentric ring developed in the period between the two SSM/I observations on 15 September. The 85-GHz imagery showed that the circular rainband structure contracted 15 km between 0900 and 2200 UTC 22 September. Figure 6c shows the time-composite radar reflectivity structure of Hugo from P-3 aircraft (courtesy of M. Black) valid at 1730 UTC. This time composite was 4.5 h prior to the SSM/I observation. The radar reflectivities depict the presence of an inner eyewall and what appeared to be a developing secondary eyewall at a larger radius. These features were similar to the SSM/I imagery seen in Fig. 6b. The large spiral rainband to the west and southwest of the hurricane was observed in both the SSM/I imagery and the aircraft radar composite. This band observed in earlier SSM/I passes was most likely the same feature that had remained quasi-stationary relative to the moving cyclone over a number of days.

At 2200 UTC 16 September, Hugo was less than 200 km from the island of Guadeloupe. The center of Hugo, as depicted in the rain-rate imagery, was denoted by the light blue circular region where rain-rate values less than 10 mm h^{-1} were observed (Fig. 6d). This region was surrounded by two tightly curved areas of precipitation with rainfall rates greater than 25 mm h^{-1}. Furthermore, the double eyewall configuration seen earlier was no longer present. The U.S. Air Force reconnaissance estimated a pressure of 941 mb during this time—an increase of 23 mb in 24 h. While an eyewall cycle may have occurred during this period, it is impossible to determine from two consecutive SSM/I rain-rate imageries if indeed this process took place. The disappearance of the inner eye usually marks the end of a period of intensification and the beginning of a weakening phase, as suggested by Willoughby et al. (1982).

During the subsequent 48 h, Hugo passed over the Leeward Islands (Fig. 2) and crossed the eastern tip of Puerto Rico. SSM/I rain-rate imagery at 2300 UTC 18 September (not shown) revealed that Hugo's precipitation pattern was less organized. Rain rates at 1000 UTC 19 September showed a large rainband extending east and south from the inner-core region (Fig. 7a). The areas of most intense rain at this time were in a semicircle extending west to east around the center.

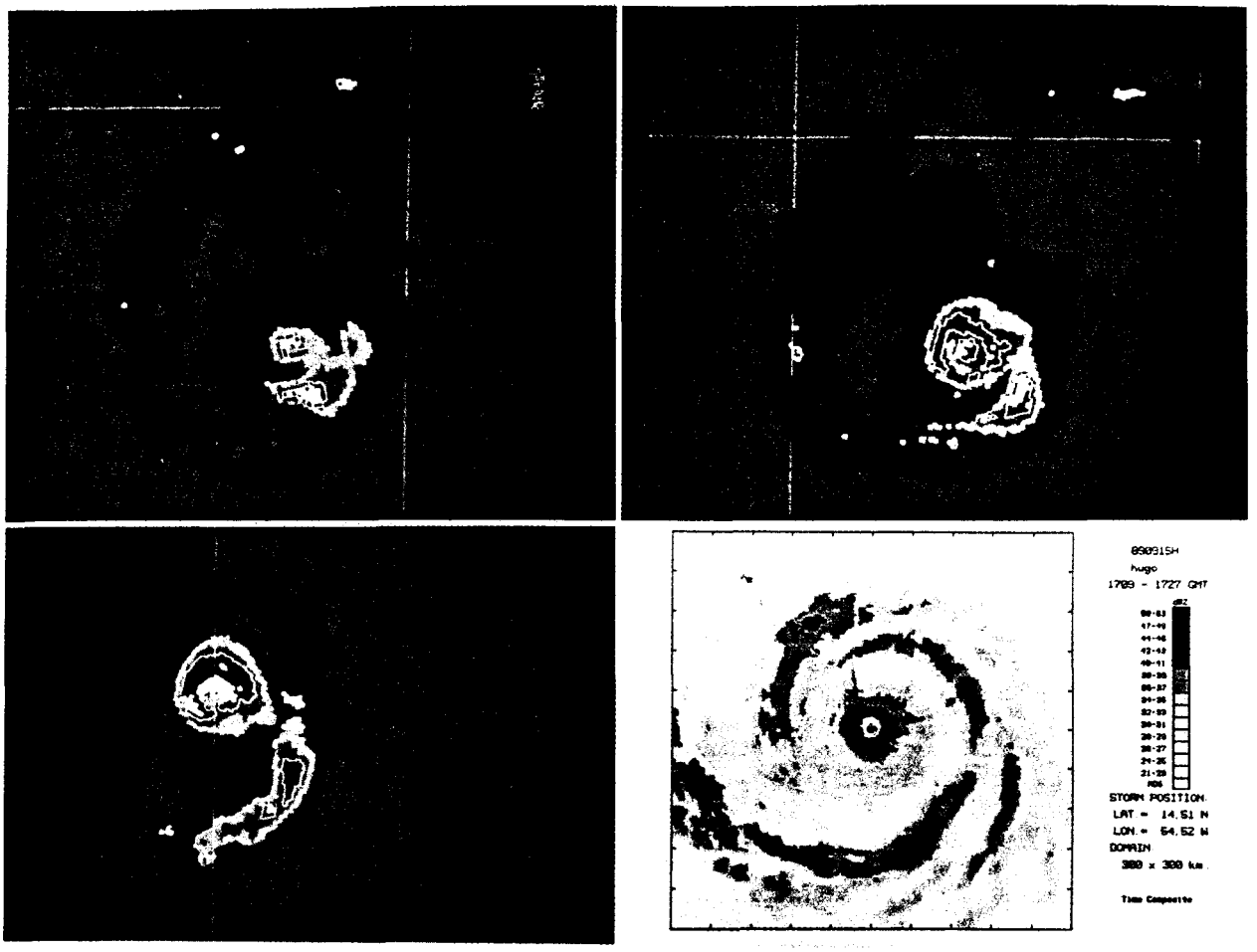

FIG. 6. (a) SSM/I rainfall rates imaged at 0900 UTC 15 September. The imagery shows a considerable increase in organization and convection around the center than in the previous image. A spiral band within the inner-core region has encompassed the center. The white horizontal–vertical lines indicate 20°N and 40°W, respectively. (b) The pass at 2200 UTC 15 September captures Hugo at near maximum intensity. The white horizontal–vertical lines indicate 20°N and 40° and 50°W, respectively. (c) Radar time composite for 1709–1727 UTC 15 September. Reflectivity intensities are denoted by shades of gray represented in the legend (image courtesy of M. Black, Hurricane Research Division–NOAA/AOML). (d) SSM/I rainfall rates at 2200 UTC 16 September. The vertical line indicates 50°W. All color rain-rate imagery shows rain rates in 5 mm h^{-1} increments. Indigo represents rates less than 5 mm h^{-1}, royal blue 5–10 mm h^{-1}, light blue 10–15 mm h^{-1}, green 15–20 mm h^{-1}, red 20–25 mm h^{-1}, and white greater than 25 mm h^{-1}.

Additionally, no intense rain rates were retrieved in the southeast quadrant of the storm. Both the effects of landfall and the presence of an upper low just south of Hispaniola may have produced some of the observed precipitation patterns by inhibiting the outflow. The pass at 2300 UTC on the same day showed that Hugo was located north of the Dominican Republic (Fig. 7b). A closed center in the rainfall pattern was observed, which was reflected by a minimum in rainfall. Rates greater than 20 mm h^{-1} were present to the east of this rainfall minimum. A large rainband emanating from the western inner-core region was also observed. Within this outer rainband, isolated areas of deep convection with high rain rates were imaged by SSM/I. The precipitation at 2300 UTC appeared to be better organized than in the SSM/I pass 13 h earlier (Fig. 7a).

Hugo's precipitation pattern was again determined by an SSM/I pass at 0000 UTC 22 September. During this pass, the center of the storm was 200 km southeast of Charleston, South Carolina. Rain rates greater than 25 mm h^{-1} were observed in a partial circle in the northern quadrants of the eyewall around a region of low rainfall rates (Fig. 8a). This region of low rain rates was approximately coincident with U.S. Air Force reconnaissance estimates of the storm center. A large rainband connected to the inner-core region of Hugo was also noted during this pass with embedded areas of rain rates greater than 20 mm h^{-1}. Figure 8b shows the southeast composite radar centered at Charleston.

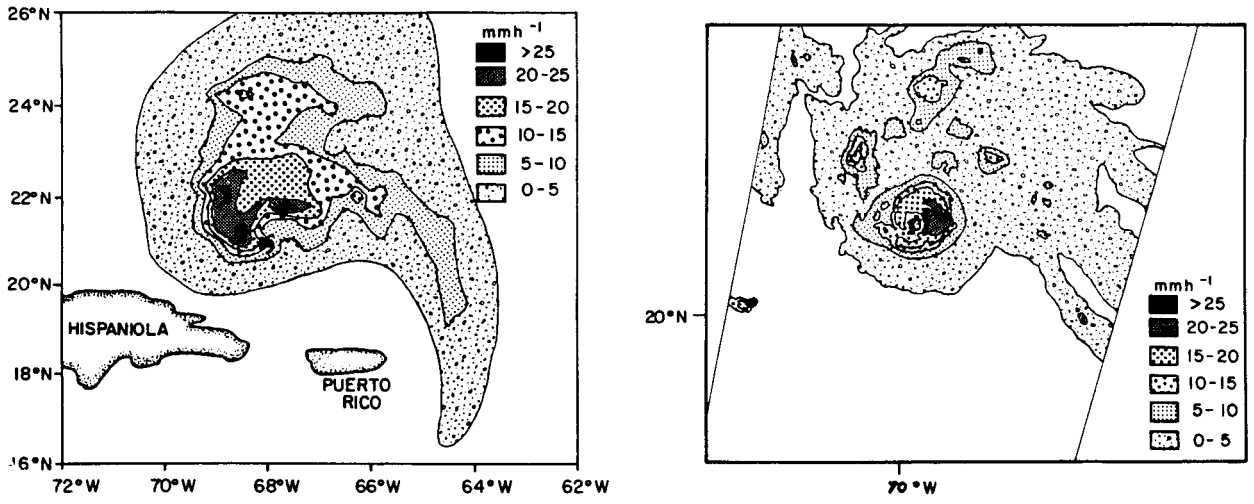

FIG. 7. (a) SSM/I rainfall rates at 1000 UTC 19 September, depict Hugo several hundred kilometers to the north of Puerto Rico. The deepest convection at this time is confined to the north and west of the center of circulation. (b) The ascending pass at 2300 UTC 19 September reveals newly formed convection to the east of the center.

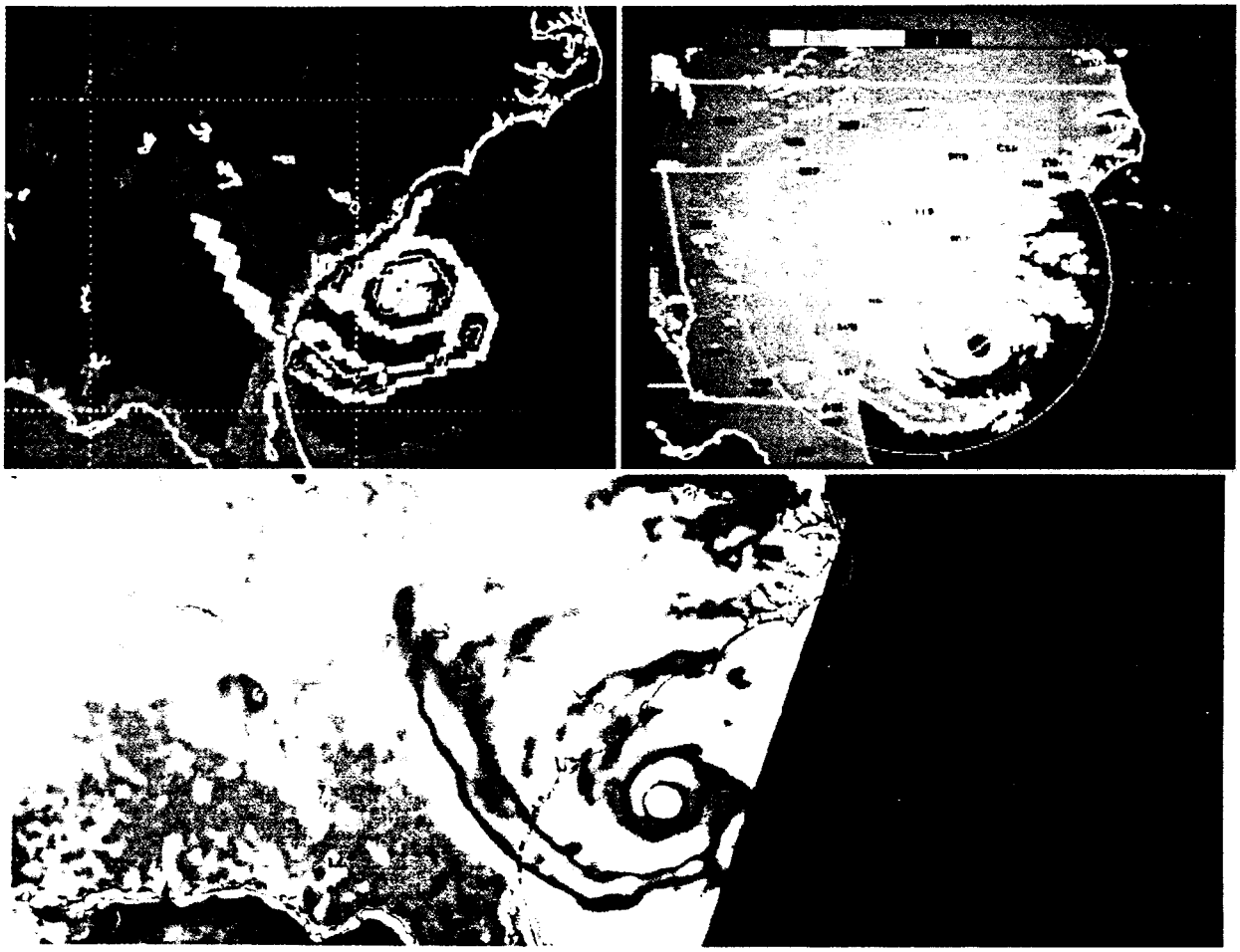

FIG. 8. (a) SSM/I rainfall rates (0000 UTC 22 September), 4 h prior to landfall. (b) Southeast radar composite at 0000 UTC 22 September reveals a similar pattern to the SSM/I rainfall rates. The legend at the top refers to the VIP levels indicating precipitation intensity. (c) SSM/I 85 GHz at 0000 UTC 22 September. Blue and turquoise shades indicate areas of deep convection. Areas shaded in white represent low-precipitating regions, like within the eye of Hugo.

The digital video integrator processor (DVIP) levels are indicated by the color code at the top of Fig. 8b. Radar observations and SSM/I rainfall rates showed a similar structure of the mesoscale rainfall patterns. In particular, the heavy precipitation occurring in the eyewall region, and the heavy rain observed in the rainband southeast of Savannah, Georgia, were also observed in the SSM/I and composite radar precipitation patterns. A quantitative comparison of SSM/I rain rates with radar-estimated rain rates was not conducted for this study. Instead, a comparison of SSM/I rain rates with raingage-measured rain amounts was performed and will be discussed in the next section. The 85-GHz imagery showed the organization of Hugo's convection (Fig. 8c). The purple, light blue, and yellow shaded regions indicate where the deepest convection was taking place, which was approximately coincident with the precipitation pattern seen in the radar composite (Fig. 8b).

5. Comparison between SSM/I and raingage observations

Due to the timely overpass of the SSM/I just prior to landfall in South Carolina, a quantitative comparison of SSM/I rainfall rates with raingage data along the southeast coastline was made. The SSM/I observation at 0000 UTC 22 September was used for this comparison. A 4-h period between 0000 UTC and 0400 UTC was selected for this comparison. In order to obtain the total precipitation expected from one SSM/I observation, the rain-rate field was first interpolated to a grid with a resolution of 0.5° in longitude and latitude. Next, the entire field was moved at 1-h intervals according to the best track obtained from NHC, with the rain values at each grid point being accumulated. The precipitation pattern of Hugo was assumed to be in steady state during the period, although the actual rain pattern probably changed. Only a 1-mb drop in the central pressure was noted in the NHC best-track data between 0000 UTC and landfall.

Figure 9a shows the 4-h predicted accumulated precipitation over the area of interest following the above procedure. Also shown is the track plotted every hour over the entire period. Maximum rainfall occurred at and near the area of landfall, as well as over central Georgia, the latter associated with a highly convective rainband (Fig. 8a). Maximum values of 89 mm were estimated on the coast near Charleston, South Carolina, and about 83 mm along the southeast Georgia coastline. A minimum in rainfall was also observed extending along the Savannah River.

Hourly precipitation data throughout North and South Carolina, Georgia, Tennessee, and Virginia were obtained from hourly reporting raingage stations. The raingages were located at sites operated by the National Weather Service, the Federal Aviation Administration, and cooperative observers. Standard raingage types include Fischer–Porter, tipping bucket, and universal. Rain rates observed by surface raingages along the South Carolina coast were comparable to SSM/I rain rates. Charleston observed rain rates greater than 20 mm h^{-1} at 0000 UTC. SSM/I rain rates showed an area of 25 mm h^{-1} impinging on the Charleston coast around 0000 UTC. Observing stations in central Georgia along a quasi-stationary rainband all reported rain rates in excess of 10 mm h^{-1} around 0000 UTC. This supported SSM/I observations.

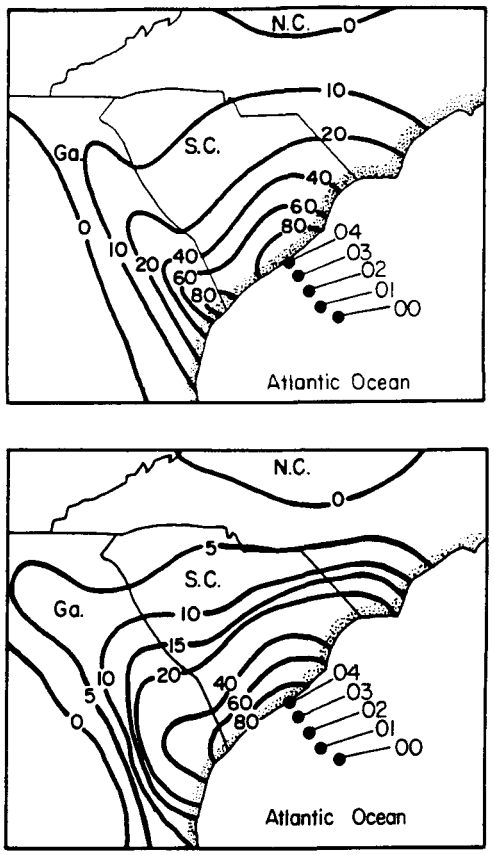

FIG. 9. (a) Four-hour SSM/I predicted rainfall (mm) for the period 0000–0400 UTC 22 September 1989. (b) Four-hour raingage totals (mm) for the same period. The track of Hugo is displayed and labeled for each hour.

Rainfall totals from raingages for the same 4-h period as the SSM/I observations were compiled and interpolated onto a grid using a two-pass Barne's scheme with a 0.5° resolution in longitude and latitude. Figure 9b shows the areal distribution of total rainfall for the 4-h period. Values in excess of 80 mm were obtained along the South Carolina coastal area near Charleston, with Charleston reporting 87 mm. These values decreased inland with increasing distance from the coastline. A slight minimum in rainfall occurred along the South Carolina and Georgia border. The observed rainfall totals over this area were similar to those predicted by SSM/I. Alliss et al. (1991) discussed in more

detail the comparison between SSM/I-derived rainfall rates and raingage observations during the time of landfall.

6. SSM/I-derived rainfall parameters

a. Total latent heat release

The total latent heat release (TLHR) was computed for eight observations for circular areas of 111-, 222-, and 444-km radius from the center of circulation. The center of circulation for all calculations was determined from an analysis of the 85-GHz imagery. The TLHR over an area is given by (Rodgers and Adler 1981)

$$\text{TLHR} = L\rho \int_A R da, \qquad (3)$$

where ρ is the density of rainwater assumed to be 1.0 $\times 10^3$ kg m^{-3}, L the latent heat of condensation (2.5 $\times 10^6$ J kg^{-1}), da the incremental area (27 km^2), R the rainfall rate at each grid point, and A the area of integration. Additionally, the ratio of the contribution of rainfall by rates greater than 10 mm h^{-1} to the total rainfall (RIP) within a 222-km radius of the center was also computed. Only passes providing full coverage within this area were chosen for the study.

The time-averaged TLHR within 111, 222, and 444 km of the center of circulation were 2.4 $\times 10^{14}$, 9.1 $\times 10^{14}$, and 16.6 $\times 10^{14}$ W, respectively. The estimate of TLHR within 444 km of the center by Rodgers and Adler (1981) for 12 observations of western Pacific typhoons was 8.7 $\times 10^{14}$ W. This difference may be due in part to the difference in the number of cases for each study, the differences in resolution of the rain rates, and the fact that Hugo was stronger than average. Additionally, all rainfall rates calculated by Rodgers and Adler were less than 10 mm h^{-1}. The estimates obtained by Rodgers and Adler, as well as ours, appear to be reasonable given the large variation in the amount of heat that tropical cyclones release.

Viewing the TLHR as a function of time is very useful in observing the intensity changes of Hugo. Figure 10 shows a plot of TLHR computed within a circular area of radius 111 km from the center for nine SSM/I passes. The top of the figure shows the maximum winds (m s^{-1}) and minimum central pressure (mb). These values were obtained from the NHC best-track data and from public advisories issued by NHC. In addition to TLHR, values of RIP were also computed.

As shown in Fig. 10, from 10 to 15 September, the value of TLHR within 111 km (TLHR111) more than doubled, increasing from 1.9 $\times 10^{14}$ W during depression stage to 4.2 $\times 10^{14}$ W observed during the 2200 UTC 15 September pass. A value of 3.0 $\times 10^{14}$ W was calculated for the 2200 UTC 16 September pass. This represented a slight decrease over the 24-h period and was coincident with a decrease in Hugo's intensity as reflected in the maximum wind and minimum pressure. Between 16 and 18 September, Hugo underwent several intensity changes, which could not be resolved by TLHR111 due to the lack of SSM/I observations during that period. Calculations performed on the two SSM/I passes of 19 September yielded values of 1.40 $\times 10^{14}$ and 1.45 $\times 10^{14}$ W, respectively. Hugo's intensity also remained unchanged during this day, as suggested by the minimum pressure and maximum wind. Between 0000 UTC 19 September and 0000 UTC 22 September, Hugo reintensified, which was also reflected in the increase of TLHR111. A value of 2.95 $\times 10^{14}$ W was reached for the 0000 UTC 22 September pass.

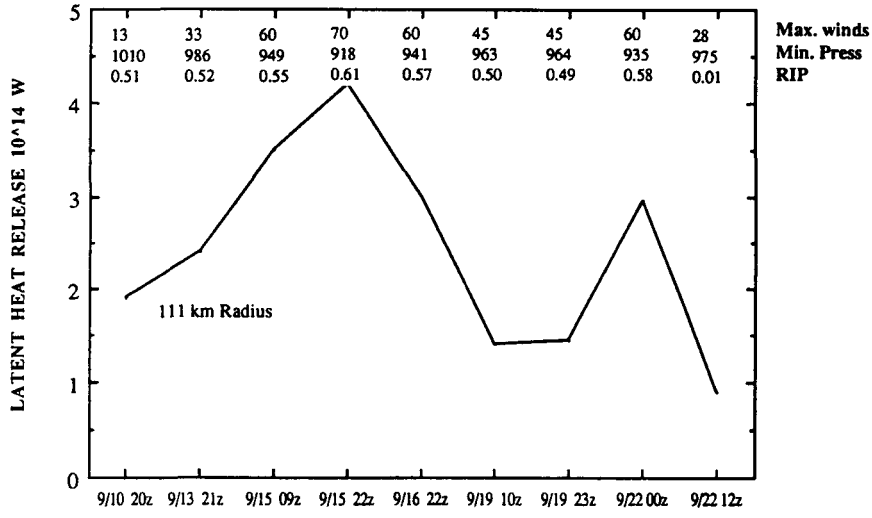

FIG. 10. Total latent heat release (TLHR) as a function of time. Calculations are for a circular area of 111-km radius from the center. Maximum wind (m s^{-1}), minimum pressure (mb), and the fraction of rainfall contributed by rainfall rates greater than 10 mm h^{-1} (RIP) are also displayed as a function of time. Wind and pressure information obtained from the NHC best-track data.

The TLHR111 of the SSM/I pass 8 h after landfall (1200 UTC 22 September) yielded a value of 0.9 $\times$ 10^{14} W. The sudden drop in TLHR during this 12-h period was most likely due to the landfall of Hugo at 0400 UTC. Rodgers and Adler (1981), who performed similar calculations, observed a 24-h lag between the maximum TLHR and intensity. Rodgers et al. (1991) found a lag of 32 h between the convective enhancement and intensity for Hurricane Irene (1981). Unfortunately, any lag present in Hugo's TLHR and intensity could not be determined from these SSM/I passes due to missing orbits and because the storm was sometimes located between adjacent swaths. Based on the availability of SSM/I imagery at 12 h, or longer intervals, it appeared that the TLHR were in phase with the observed intensity. Hopefully, with more frequent SSM/I observations in the future, along with reconnaissance data, a lag can be determined more definitely.

b. Other intensity parameters

The intensification of Hugo during this period was also evident in other SSM/I-derived rainfall parameters (Fig. 10). The RIP increased from 0.51 to 0.61 between 10 and 15 September. The reintensification of Hugo, which commenced 2 days prior to landfall, was also reflected in the RIP variations. RIP values increased from 0.49 to 0.58 between 2300 UTC 19 September and 0000 UTC 22 September. During this period of intensification, the central pressure of Hugo dropped approximately 30 mb (Fig. 3). A t test was conducted to determine the statistical significance between pressure and RIP. A correlation coefficient of $-.926$ was obtained and was significant at the 1% level. Thus, as Hugo's surface pressure dropped, the contribution of SSM/I-determined RIP increased. Likewise, during times of weakening, a decrease in the RIP values was observed.

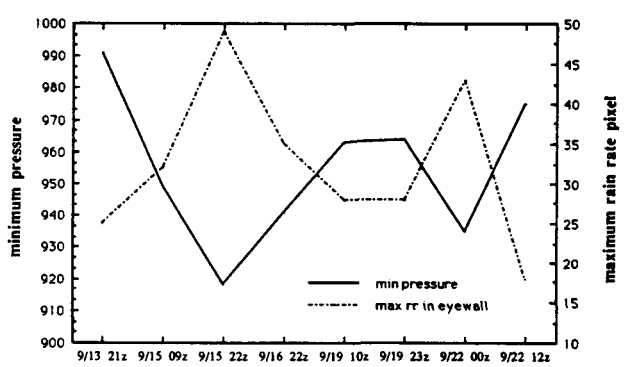

FIG. 11. Maximum rainfall rate within the eyewall region as a function of minimum central pressure. During the two maximum intensity periods, SSM/I observations show a maximum in rainfall rate within the eyewall region.

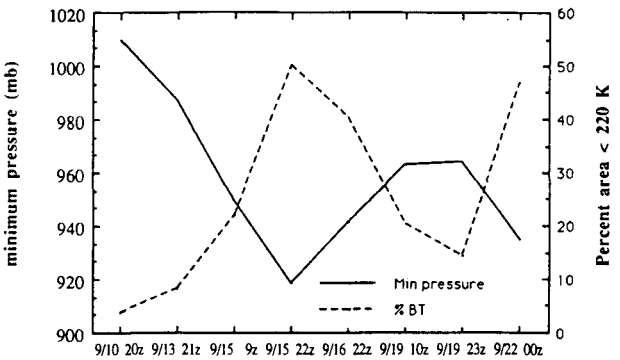

FIG. 12. Minimum central pressure (mb) and the percentage of 85-GHz brightness temperatures less than 220 K within a circular area of radius 111 km as a function of time.

Another method to relate the intensity of the storm with SSM/I rain rates was to compare the maximum SSM/I rain rate at a pixel in and near the eyewall region with the observed minimum central pressure. Only SSM/I passes where the storm was of hurricane status were used for this comparison. This was done to avoid times in which a distinct inner circulation or eyewall was not present. As shown in Fig. 11, when the central pressure in the storm decreased, the maximum rain rate observed by SSM/I increased in all cases. Two maxima in rain rate coincided with the two lowest pressure measurements. During these two passes, the maxima in rain rates were found to be 49 and 43 mm h^{-1}, corresponding to minimum pressures estimated by NHC of 918 and 935 mb, respectively. Since the temporal resolution was poor, the lag between the convection and minimum pressure could not be determined, as discussed before. A correlation coefficient between the maximum rain rate and minimum pressure was calculated to be $-.90$. This suggests a high probability that the two fields were related. Additional cases, however, are needed to verify this preliminary result and to determine the lag.

Examining the horizontally polarized 85-GHz BTs around the storm center may also be indicative of the storm's intensity. Wilheit et al. (1982) and Spencer et al. (1988) have shown that, at microwave frequencies near 85 GHz, large ice and water particles present in convective precipitation scatter the upwelling energy, resulting in cold BTs relative to the warm ocean background. As a storm intensifies, the areal coverage of deep convection around the center should increase. Because 85-GHz BTs less than 220 K are associated with heavy precipitation, a comparison between the central pressure and percentage of 85-GHz BTs less than 220 K can be examined. The calculations were performed over a circular area with a radius from the center of 111 km. Figure 12 shows that in all cases, as the central pressure decreased, the percent area of 85-GHz BT less than 220 K increased, while during times of increasing pressure, a decrease in the percentage was

TABLE 1. Percent areal coverage of rainfall and the percent contribution of rainfall (in parentheses) for four rainfall-rate categories (mm h^{-1}) within a radius of 200 km from the center during an intensification episode. Also shown are the minimum central pressures (mb) observed during each time.

SSM/I pass	Minimum pressure	SSM/I rainfall rates			
		<5	5–15	15–25	>25
1000 UTC 10 September	1010	67 (47)	25 (33)	8 (20)	0 (0)
0900 UTC 15 September	949	39 (13)	47 (55)	11 (24)	3 (8)
2200 UTC 15 September	918	32 (6)	35 (38)	28 (46)	5 (10)

noted. A correlation of −.93 was found between the two parameters at the 0.4% confidence level. Felde and Glass (1991) found similar behavior for western Pacific typhoons during both intensification and weakening stages.

7. Rain-rate statistics

a. General characteristics

The contributions of rainfall within specified rain-rate categories and the areal coverage of these rain rates were examined during a period of intensification. The objective was to see how the contribution and areal coverage of rainfall changed during these times. Table 1 shows the percent areal coverage of rainfall and the percent contribution of rainfall (in parentheses) for four rain-rate categories within 200 km of the center. In addition, the central pressures obtained from NHC best-track data are shown for comparison purposes. Figure 2 shows the pressure decrease that took place between 10 and 15 September. The SSM/I observation (1000 UTC 10 September) during tropical-depression stage showed that there was little organization of the storm's convection. Table 1 shows that rain rates less than 5 mm h^{-1} occur in 67% of the area and contribute approximately 47% to the total rainfall during this period. No rain rates greater than 25 mm h^{-1} were observed during depression stage. The second SSM/I observation (0900 UTC 15 September) showed that rates less than 5 mm h^{-1} now occurred only in 39% of the area. The increasingly important contribution of heavier precipitation was evident at this time. Rates greater than 25 mm h^{-1} occurred in 3% of the area and contributed to 8% of the total rainfall. The third observation of Hugo, 13 h later (2200 UTC 15 September), showed an even larger contribution of rates greater than 15 mm h^{-1}. Rates less than 5 mm h^{-1} occurred in only 32% of the area, as compared to 67% of the area during the first observation. Precipitation with intensity between 15 and 25 mm h^{-1} occurred in 28% of the area, but contributed to 46% of the total. By 2200 UTC, Hugo's intensity had peaked. It appears that as the storm intensified, there was a shift toward heavier precipitation within the radius of 200 km. These observations were also consistent with the RIP values, which showed the contribution of rates greater than 10 mm h^{-1} to the total storm rainfall.

b. Spatial variations of rainfall

Rainfall rates averaged over time and space were calculated for four circular areas with radii 60, 111, 222, 333, and 444 km from the center. Data from six SSM/I overpasses during hurricane stage were used. The time-averaged mean rain rate within these circular areas was 14.5, 12.1, 8.8, 5.6, and 4.0 mm h^{-1}, respectively. Large variations of these rain rates existed for individual times according to the observed intensity during that period. Within 60 km of the center, precipitation averaged from a minimum of 5.9 mm h^{-1} to a maximum of 19.5 mm h^{-1} observed at 0900 UTC 15 September. Marks (1985) points out that the average rain rate in the eyewall of Hurricane Allen increased as the eyewall radius decreased during the concentric eyewall cycle described by Willoughby et al. (1982). Due to the coarse resolution of SSM/I rainfall rates (25 km), compared to that of radar data (used by Willoughby 1982), a determination of whether or not the rain rate increased with decreasing eyewall radius was impossible.

The average spatial distribution of rainfall rate as a function of distance from the center of circulation was computed for various stages of development. Additionally, the average rainfall rate by quadrant oriented relative to the storm track was also computed. Figure 13 shows the average rainfall rate for each 20-km radius from the center during the intensification phase between 10 and 15 September. The figure shows that as Hugo intensified, the maximum average rainfall rate increased. It is evident that the convection surged toward smaller radii between 10 and 15 September. Due to the lack of SSM/I observations between these times, however, the detailed fashion of the contraction could not be determined. We do note, however, that the maximum average rain rate increased from 9 mm h^{-1} at depression stage at a radius of 50 km to 19 mm h^{-1} during the hurricane stage at a radius of 30 km. During the 2200 UTC 15 September pass there were three separate maxima in rainfall rates. Values of 16, 14.5, and 15 mm h^{-1} were observed at a radius of 30, 70, and 130 km, respectively. The inner two maxima supported

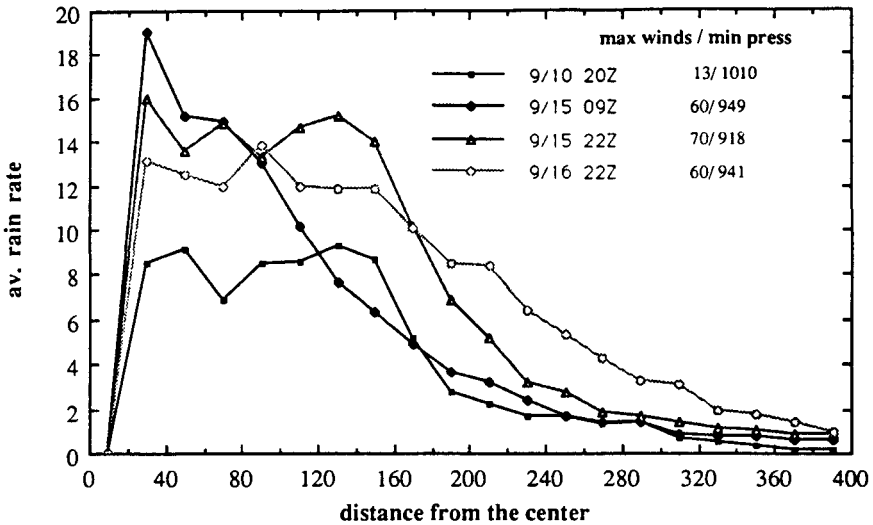

FIG. 13. (a) Mean rainfall rate (mm h^{-1}) as a function of radial distance (km) from the center during the intensification period that occurred between 10 and 15 September.

the observation of two concentric convective rings that were observed in the SSM/I imagery and in the P-3 radar composite (Figs. 6b,c). The SSM/I rain-rate imagery 24 h later (2200 UTC 16 September) showed that the two concentric rings no longer existed. This was also evident in Fig. 13, which showed a single maximum rain rate of 14 mm h^{-1} at a radius of 90 km.

The time-averaged rain rate by quadrant within 75 km of the center relative to the storm motion is shown in Fig. 14. These values are averages of six observations of Hugo during the hurricane stage. The numbers in parentheses represent the standard deviations for each quadrant. The distribution is such that 30% of the total rainfall occurred in the left front (LF) quadrant and 26% occurred in the right front (RF) quadrant. It appears that the rain rates in both the left rear (LR) and right rear (RR) quadrants fluctuated much less than those in the other quadrants, with standard deviations of 3.5 and 3.2 mm h^{-1}, respectively. This was much less than those for the LF and RF quadrants. This suggests that the front semicircle (in the direction of motion) had more rain intensity changes than the rear semicircle. Burpee and Black (1989) suggest that translational speeds of hurricanes appear to be one of several factors that may determine the orientation of the precipitation patterns. Shapiro (1983) found that the axisymmetric convection distribution within the eyewall was related to the asymmetries in the boundary-layer convergence, which in turn was associated with the translation of the storm. Since Hugo had translational speeds ranging from 3 to greater than 10 m s^{-1}, storm motion may have caused the particular distribution shown here.

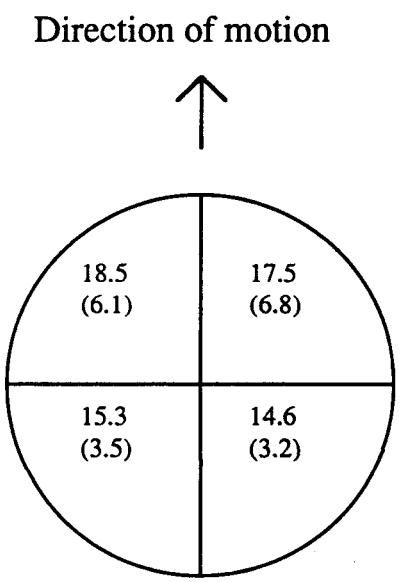

FIG. 14. Time-averaged rainfall rate (mm h^{-1}) and standard deviations (in parentheses) for a circular area of radius 75 km from the center, viewed by quadrant, relative to the storm motion.

8. SSM/I center fixing

Velden et al. (1989) and Sandlin and Spangler (1989) have both shown the usefulness of 85-GHz imagery in locating the centers of tropical cyclones. Additionally, NHC began processing 85-GHz data during October 1989, and has developed several applications for its use. Rappaport (1991) points out that the data has, in general, been accepted for operational use. For this study, nine cases were examined. An estimation of the location of the center was determined in several ways. If no eye was present, the estimate from the 85-

GHz imagery was made by locating the center of the low-level circulation as defined by the tightly wrapped convection near the storm center. If an eye was present, not only was the location of such a center estimated, but the maximum BT in that region was also located. Figure 15a shows the 85-GHz imagery of Hugo around 1000 UTC 19 September. Figure 15b shows the GOES enhanced infrared image for the same time (GOES visible imagery was unavailable due to darkness). The SSM/I image showed a tightly curved convective band to the north of Puerto Rico, just northeast of 21.0°N, 68.0°W. This location was approximately coincident with the NHC public advisory, which indicated that the center of Hugo was at about 21.2°N, 67.7°W near

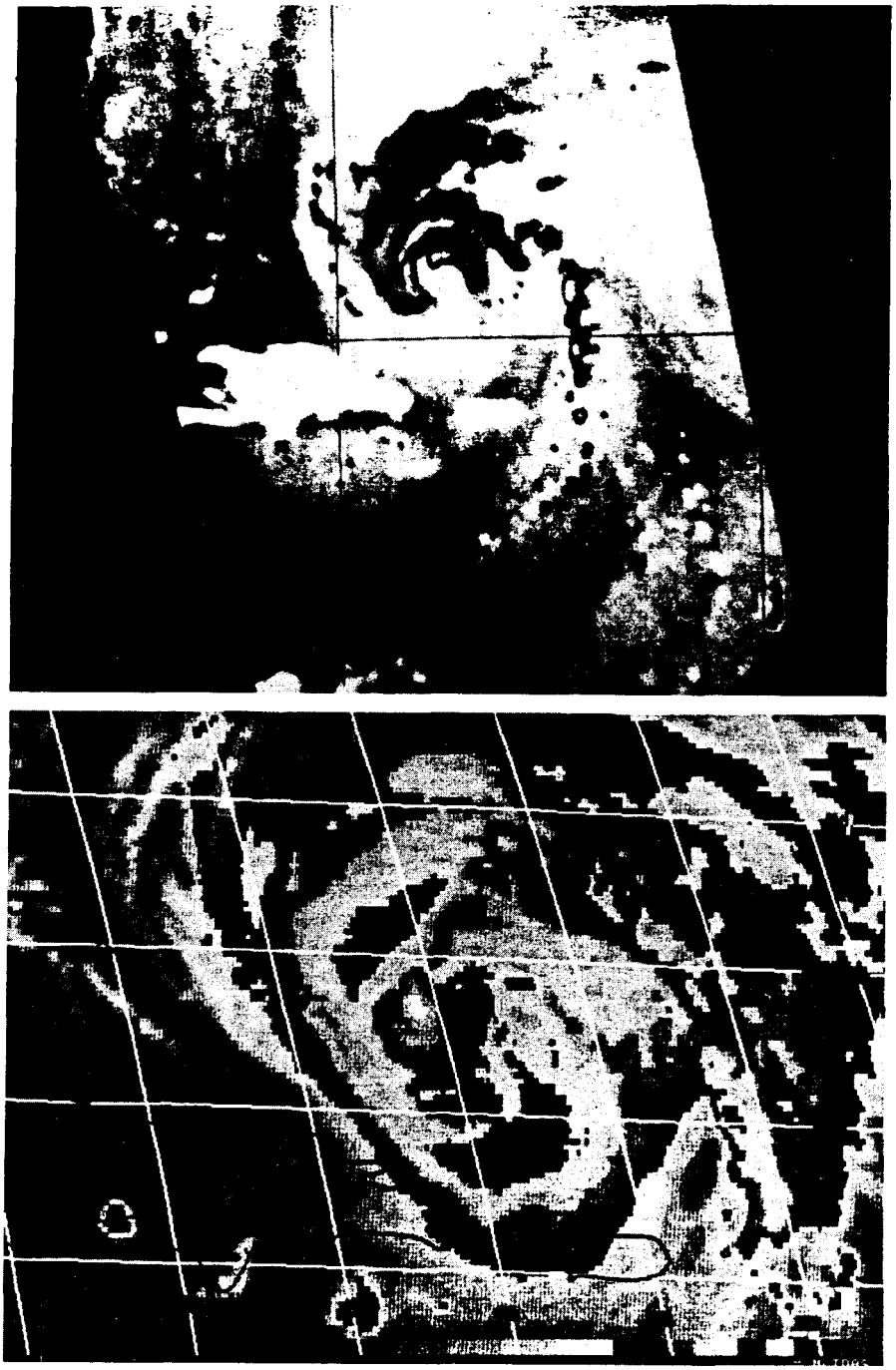

FIG. 15. Hurricane Hugo at 1000 UTC 19 September 1989, as seen by (a) SSM/I 85-GHz imagery and (b) GOES infrared imagery.

TABLE 2. The average difference (km) between the NHC low-level center, extrapolated to SSM/I time, and the center estimated from SSM/I 85-GHz imagery.

NHC method of determination	NHC-SSM/I difference (km)
GOES only (three cases)	32
Reconnaissance and GOES (six cases)	12
Combined average (nine cases)	18

1000 UTC. Neither the banding areas of convection nor the center could be inferred in the GOES imagery. The infrared image was dominated by a large area of cirrus clouds obscuring the center.

A comparison was made between the NHC best-track positions and the estimated SSM/I center (Table 2). These positions were determined from reconnaissance and satellite measurements. All NHC positions were extrapolated to the time the SSM/I scan crossed the position of the proposed center (SSM/I time). The extrapolation was conducted using the NHC advisories, which contained information on speed and direction of movement. The extrapolation did not take into account unsteady motion between best-track positions or for trochoidal motions; thus, some error may have been introduced. The extrapolations performed, however, did not exceed 1 h; therefore, any bias is assumed to be small. As listed in Table 2, the average difference between SSM/I and NHC estimates, when reconnaissance information was not available, was 32 km. This average dropped to 12 km when the NHC estimate used information from reconnaissance flights. This suggests that SSM/I estimations of the low-level center were more comparable to NHC estimates when reconnaissance information was available at NHC. For all nine observations, the average difference was 18 km. While limited in availability and subject to image interpretation, SSM/I 85-GHz imagery may provide supplemental information to enhance existing satellite capabilities. This preliminary examination also suggests a potential for reduced positioning errors, especially during times when high clouds cover the system's low-level center.

9. Conclusions

Data from the SSM/I on board the DMSP F-8 spacecraft have been used to study the various storm-structure features observed in Hugo. Rainfall rates and 85-GHz imagery were instrumental in observing Hugo's convective organization and precipitation patterns. Assuming data becomes available at shorter time intervals, a potentially valuable application of SSM/I might be to estimate minimum central pressure and maximum winds from the rain-rate imagery, analogous to the Dvorak (1975) technique. Additionally, rainfall rates measured by SSM/I just prior to landfall strongly support those observed at reporting stations along the Georgia–South Carolina coastlines. These results indicate that rain data obtained by SSM/I may be useful in providing forecasts for precipitation amounts over coastal areas as tropical cyclones make landfall.

It was found that the TLHR calculated from SSM/I rainfall rates was comparable to estimates made by Rodgers and Adler (1981), who studied other tropical cyclones using the Nimbus Electrically Scanning Microwave Radiometer (ESMR-5). Furthermore, observations showed that as the TLHR increased with time, so did the intensity of Hugo. Because of the poor temporal resolution, any lag present between the TLHR and the intensity was impossible to determine. The contribution of heavier rainfall rates to the total storm rainfall (RIP) was calculated and observed to increase as Hugo intensified. It was found that higher rainfall rates occurred closer to the inner-core region during times of intensification. The areal coverage of higher rainfall rates was also observed to increase during times of intensification. Maximum rainfall rates in the eyewall region were found to increase as the minimum observed central pressure decreased. Poor temporal resolution prevented an estimation of the lag between the convection and minimum pressure. With three sensors currently in orbit, more frequent observations of tropical cyclones might help in determining this lag time.

The utility of SSM/I 85-GHz imagery in estimating the location of the low-level circulation has also been demonstrated in this study. The usefulness of SSM/I data for this application was most beneficial when the eye of Hugo was obscured by clouds and at night when GOES visible imagery was unavailable. Furthermore, in the event that GOES becomes inoperative, or during times when no airborne reconnaissance data is available, SSM/I observations may become increasingly important for operational use.

Acknowledgments. We thank Glenn Sandlin of Naval Research Laboratory for processing the SSM/I data, for providing us with the SSM/I imagery, and for invaluable discussions on the SSM/I data characteristics. We also wish to thank Kevin Schrab and Ronald Weglarz of North Carolina State University for their helpful suggestions. This research was supported by an NRL Basic Research Grant and ONR Grant N0001492AF00002.

REFERENCES

Adler, R. F., and E. B. Rodgers, 1977: Satellite-observed latent heat release in a tropical cyclone. *Mon. Wea. Rev.*, **105**, 956–963.

Alliss, R. A., S. Raman, and S. W. Chang, 1991: A comparison of rainfall rates and intensity during Hurricane Hugo using SSM/I observations. *Proc., 19th Conf. on Hurricanes and Tropical Meteorology*, Miami, Amer. Meteor. Soc., 391–395.

Black, P. G., and F. D. Marks, 1991: The structure of an eyewall meso-vortex in Hurricane Hugo (1989). *Proc., 19th Conf. on Hurricanes and Tropical Meteorology*, Miami, Amer. Meteor. Soc., 579–582.

Burpee, R. W., and M. L. Black, 1989: Temporal and spatial variations of rainfall near the centers of two tropical cyclones. *Mon. Wea. Rev.*, **117**, 2204–2209.

Case, R. A., and M. B. Mayfield, 1990: Atlantic hurricane season of 1989. *Mon. Wea. Rev.*, **118**, 1171–1175.

Dvorak, V. R., 1975: Tropical cyclone intensity analysis and forecasting from satellite imagery. *Mon. Wea. Rev.*, **103**, 420–430.

Felde, G. W., and M. Glass, 1991: SSM/I brightness temperatures analysis of tropical cyclones. *Proc., 19th Conf. on Hurricanes and Tropical Meteorology*, Miami, Amer. Meteor. Soc., 400–404.

Goodberlet, M. A., C. T. Swift, and J. C. Wilkerson, 1989: Remote sensing of ocean surface winds with the Special Sensor Microwave/Imager. *J. Geophys. Res.*, **94**, 547–555.

Hollinger, J. P., 1989: DMSP Special Sensor Microwave/Imager Calibration Validation. Final Report, Vol. I, 51 pp. [Available from J. P. Hollinger, Naval Research Laboratory, Washington, DC 20375.]

——, 1991: DMSP Special Sensor Microwave/Imager Calibration Validation. Final Report, Vol. II, 106 pp. [Available from J. P. Hollinger, Naval Research Laboratory, Washington, DC 20375.]

Marks, F. D., Jr., 1985: Evolution of the structure of precipitation in hurricane Allen (1980). *Mon. Wea. Rev.*, **113**, 1268–1285.

Mayfield, M., C. J. McAdie, and A. Pike, 1988: A preliminary evaluation of the dispersion of tropical cyclone position and intensity estimates determined from satellite imagery. NOAA National Hurricane Center Research Paper, 16 pp.

Negri, A. J., R. F. Adler, and C. D. Kummerow, 1989: False-color display of Special Sensor Microwave/Imager (SSM/I) data. *Bull. Amer. Meteor. Soc.*, **70**, 146–151.

Olson, W. S., 1989: Physical retrieval of rainfall rates over the ocean by multispectral microwave radiometry-application to tropical cyclones. *J. Geophys. Res.*, **94**, 2267–2280.

Powell, M. D., P. P. Dodge, and M. L. Black, 1992: The landfall of Hurricane Hugo in the Carolinas, *Wea. Forecasting*, **6**, 379–399.

Rao, G. V., P. D. MacArthur, and J. H. McCoy, 1991: The SSM/I latent heat release and brightness temperature anomalies associated with tropical cyclones and their utility in predicting intensity changes of tropical storms. *Proc., 19th Conf. on Hurricanes and Tropical Meteorology*, Miami, Amer. Meteor. Soc., 175–178.

Rappaport, E. N., 1991: Operational applications of SSM/I data at the National Hurricane Center. *Proc., 19th Conf. on Hurricanes and Tropical Meteorology*, Miami, Amer. Meteor. Soc., 179–183.

——, and P. G. Black, 1989: The utility of Special Sensor Microwave/Imager data in the operational analysis of tropical cyclones. *Proc., Fourth Conf. on Satellite Meteorology and Oceanography*, San Diego, Amer. Meteor. Soc., J21–J24.

Rodgers, E. B., and R. F. Adler, 1981: Tropical cyclone rainfall characteristics as determined from a satellite passive microwave radiometer. *Mon. Wea. Rev.*, **109**, 506–521.

——, S. Chang, J. Stout, J. Steranka, and J. J. Shi, 1991: Satellite observations of variations in tropical cyclone convection caused by upper-tropospheric troughs. *J. Appl. Meteor.*, **30**, 1163–1184.

Sandlin, G. D., and D. J. Spangler, 1989: SSM/I imagery, center-fixes, and wind fields for tropical cyclones. Naval Research Laboratory Report, 18 pp. [Available from G. D. Sandlin, Naval Research Laboratory, Washington, D.C. 20375.]

Shapiro, L. J., 1983: The asymmetric boundary layer flow under a translating hurricane. *J. Atmos. Sci.*, **40**, 1984–1998.

Spencer, R. W., H. M. Goodman, and R. E. Hood, 1989: Precipitation retrieval over land and ocean with the SSM/I: Identification and characteristics of the scattering signal. *J. Atmos. Oceanic Technol.*, **6**, 254–273.

Velden, C. S., W. S. Olson, and B. A. Roth, 1989: Tropical cyclone center-fixing using SSM/I Data. *Proc., Fourth Conf. on Satellite Meteorology and Oceanography*, San Diego, Amer. Meteor. Soc., J36–J39.

Wilheit, T. T., A. T. C. Chang, J. L. King, E. B. Rodgers, R. A. Nieman, B. M. Drupp, A. S. Milman, J. S. Stratigos, and H. Siddalingaiah, 1982: Microwave radiometric observations near 19.35, 92, and 183 GHz of precipitation in Tropical Storm Cora. *J. Appl. Meteor.*, **21**, 1137–1145.

Willoughby, H. E., J. A. Clos, and M. G. Shoreibah, 1982: Concentric eye walls, secondary wind maxima, and the evolution of the hurricane vortex. *J. Atmos. Sci.*, **39**, 395–411.

——, F. D. Marks, Jr., and R. J. Feinberg, 1984: Stationary and moving convective bands in hurricanes. *J. Atmos. Sci.*, **41**, 3189–3192.

Reprinted from MONTHLY WEATHER REVIEW, Vol. 120, No. 12, December 1992
American Meteorological Society